Intrinsic anomalous Hall effect across the magnetic phase transition of a spin-orbit-coupled Bose-Einstein condensate

Canhao Chen,[1,2,3,*] Guan-Hua Huang,[4,1,*] and Zhigang Wu[1,2,3,†]

[1]*Shenzhen Institute for Quantum Science and Engineering, Southern University of Science and Technology, Shenzhen 518055, China*
[2]*International Quantum Academy, Shenzhen 518048, China*
[3]*Guangdong Provincial Key Laboratory of Quantum Science and Engineering, Southern University of Science and Technology, Shenzhen 518055, China*
[4]*Department of Physics, Southern University of Science and Technology, Shenzhen 518055, China*

(Received 4 December 2022; accepted 17 April 2023; published 28 April 2023)

We study theoretically the zero-temperature intrinsic anomalous Hall effect in an experimentally realized two-dimensional spin-orbit-coupled Bose gas. For anisotropic atomic interactions and as the spin-orbit-coupling strength increases, the system undergoes a ground-state phase transition from states exhibiting a total in-plane magnetization to those with a perpendicular magnetization along the z direction. We show that finite frequency, or ac, Hall responses exist in both phases in the absence of an artificial magnetic field, as a result of finite interband transitions. However, the characteristics of the anomalous Hall responses are drastically different in these two phases because of the different symmetries preserved by the corresponding ground states. In particular, we find a finite dc Hall conductivity in one phase, but not the other. The underlying physical reasons for this are analyzed further by exploring relations of the dc Hall conductivity to the system's chirality and Berry curvatures of the Bloch bands. Finally, we discuss an experimental method of probing the anomalous Hall effect in trapped systems.

DOI: 10.1103/PhysRevResearch.5.023070

I. INTRODUCTION

The attempts to understand the origins of various nonordinary Hall effects have played an important role in establishing the field of electronic topological materials [1–3]. Indeed, the famous work by Thouless *et al.* [4], which was the first to introduce the concept of a topological invariant for magnetic Bloch bands, originated from an analysis of the integer quantum Hall effect. Another phenomenon that has generated great interest in the context of topological materials is the anomalous Hall effect (AHE) [5,6], which refers to strong Hall responses in the absence of a magnetic field and was originally discovered in ferromagnetic materials with spin-orbit (SO) couplings. Central to the study of both effects is the idea that the Bloch bands occupied by the electrons have nontrivial geometric and topological features which can significantly affect transport properties such as the Hall conductivity [6].

In recent years, much progress has been made in the area of quantum gases to generate such band structures [7], by introducing artificial magnetic fields, engineering synthetic spin-orbit couplings, or some other means. In addition to simulations of noninteracting fermionic topological phases [8–11], this has enabled the creation of bosonic topological systems where atomic interactions are essential for the emergence of topological properties [12–25]. In parallel, many probing methods have also been devised and implemented to measure the transport properties of the quantum gas systems [26–28]. These developments have led us to ask whether nontrivial Hall responses such as the AHE can be found in these bosonic topological systems and, if so, how they can be detected in experiments. In the context of charge-neutral atomic gases, the AHE refers to the phenomenon where the application of a uniform force induces a transverse current, in the absence of an artificial magnetic field [29]. Indeed, some of us have recently predicted [30] that a ground-state AHE exists in a bosonic chiral superfluid in a boron nitride optical lattice [25] and may be probed with currently available experimental techniques. Here the AHE is intrinsic as the cold atomic system is naturally free of impurities. Indeed, we have shown that the superfluid's chirality and the Berry curvature of the condensate mode are two factors underlying the intrinsic AHE [30].

The main purpose of this paper is to apply the ideas and methods developed in Ref. [30] to investigate another recently realized bosonic topological system, a two-dimensional (2D) spin-orbit-coupled (SOC) Bose gas in an optical lattice [22]. As we are interested in the AHE, we focus on the situation where the Zeeman field is absent. In this case, it was shown earlier that the interplay of atomic interactions and the SOC can give rise to nontrivial excitation band topology as well as gapless edge states [31], both of which are also found in

*These authors contributed equally to this work.
†wuzg@sustech.edu.cn

the bosonic chiral superfluid [25]. More importantly, a careful analysis of the ground states of the SOC system shows that it carries a finite, global angular momentum in one of the phases, making it also a chiral superfluid similar to that in Ref. [25]. Motivated by these similarities, we perform a systematic calculation on the ground-state Hall conductivity of the SOC system and reveal surprisingly even richer phenomenology of the AHE compared to the chiral superfluid studied in Ref. [30].

The rest of the paper is organized as follows. In Sec. II, we provide a detailed discussion of the system's Hamiltonian and the various symmetries exhibited by the Hamiltonian. In Sec. III, we calculate the ground state of the system and demonstrate the existence of a magnetic phase transition driven by the spin-orbit-coupling strength. The two magnetic phases are distinguished not only by different directions of the magnetization, but, more importantly, by different symmetries preserved by the ground state. The consequence of these distinctions are explored in Sec. IV in the context of the anomalous Hall effect, where we find contrasting structures of the ac Hall conductivity in these two phases. In particular, the dc Hall conductivity is finite in the perpendicular magnetization phase, but vanishes in the in-plane magnetization phase. The underlying causes for this are analyzed in Sec. V. In Sec. VI, we discuss an experimental proposal to observe the intrinsic AHE in the SOC system using the center-of-mass oscillations. The main results are summarized again in Sec. VII.

II. QUASI-2D SPIN-ORBIT-COUPLED BOSE GAS

A. Hamiltonian

The system of interest is a quasi-2D two-component Bose gas confined in a square optical lattice potential, where a robust spin-orbit coupling is realized by means of a Raman lattice scheme [22]. Our model is based on the system implemented by Ref. [22], although the effect of a trapping potential is not considered for the moment. The noninteracting part of the Hamiltonian is

$$\hat{H}_0 = \int d\boldsymbol{r}\, \hat{\boldsymbol{\psi}}^\dagger(\boldsymbol{r}) h_0 \hat{\boldsymbol{\psi}}(\boldsymbol{r}). \tag{1}$$

Here we adopt a spinor notation $\hat{\boldsymbol{\psi}} = (\hat{\psi}_\uparrow, \hat{\psi}_\downarrow)^T$, where $\hat{\psi}_\sigma$ is the field operator with $\sigma = \uparrow, \downarrow$ as the spin index. The single-particle Hamiltonian is given by

$$h_0 = \left[\frac{\boldsymbol{p}^2}{2m} + V_{\text{latt}}(\boldsymbol{r})\right] I + V_{R,1}(\boldsymbol{r})\sigma_x + V_{R,2}(\boldsymbol{r})\sigma_y, \tag{2}$$

where I is the unit matrix in the spin space and σ_x, σ_y are Pauli matrices. Here, $V_{\text{latt}}(\boldsymbol{r}) = V_0(\cos^2 k_L x + \cos^2 k_L y)$ is the 2D square optical potential with lattice depth V_0 and lattice spacing π/k_L [see Fig. 1(a)]; $V_{R,1}(\boldsymbol{r}) = M_0 \sin(k_L x)\cos(k_L y)$ and $V_{R,2}(\boldsymbol{r}) = M_0 \sin(k_L y)\cos(k_L x)$ are the Raman potentials coupling the spin to the motional degrees of freedom [see Figs. 1(c) and 1(d)], where the coupling strength M_0 can be experimentally tuned. The Raman lattices are commensurate with the square optical lattice, but have a unit cell twice as large. The primitive vectors of the composite lattice potential are thus given by those of the Raman lattices, i.e., $\boldsymbol{a}_1 = \pi/k_L(1, 1)$ and $\boldsymbol{a}_2 = \pi/k_L(-1, 1)$. The original square lattice can then be divided into two sublattices, A and B, distinguished by the local Raman potentials around the lattice sites. Note that we have not included any Zeeman field in Eq. (2) in order to explore effects in which the atomic interactions play a fundamental role. The latter are described by

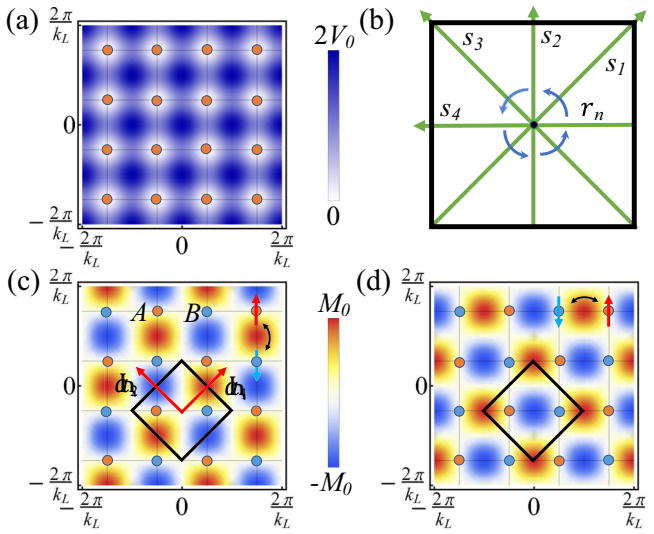

FIG. 1. (a) Illustration of the optical square lattice potential. (b) The dihedral point group symmetry D_4 for the single-particle Hamiltonian in the absence of the Raman potentials. (c), (d) Illustrations of the Raman potentials $V_{R,1}(\boldsymbol{r})$ and $V_{R,2}(\boldsymbol{r})$, respectively. The Wigner-Seitz cell and primitive vectors of the Raman potentials are also shown.

$$\hat{H}_{\text{int}} = \frac{1}{2}\sum_{\sigma\sigma'} g_{\sigma\sigma'} \int d\boldsymbol{r}\, \hat{\psi}^\dagger_\sigma(\boldsymbol{r})\hat{\psi}^\dagger_{\sigma'}(\boldsymbol{r})\hat{\psi}_{\sigma'}(\boldsymbol{r})\hat{\psi}_\sigma(\boldsymbol{r}), \tag{3}$$

where $g_{\sigma\sigma'}$ are species-dependent interaction strengths. We shall consider the case of anisotropic interactions found in experiments, more specifically the case where the intraspecies interaction strengths $g_{\uparrow\uparrow} = g_{\downarrow\downarrow}$ are greater than the interspecies ones $g_{\uparrow\downarrow} = g_{\downarrow\uparrow}$. As we shall see later, for such an interaction, the system experiences a ground-state magnetic phase transition as the spin-orbit-coupling strength increases. For the purpose of symmetry analysis, it is useful to rewrite Eq. (3) as

$$\hat{H}_{\text{int}} = \frac{1}{2}\int d\boldsymbol{r} : [\bar{g}(\hat{\boldsymbol{\psi}}^\dagger\hat{\boldsymbol{\psi}})^2 + \delta g(\hat{\boldsymbol{\psi}}^\dagger\sigma_z\hat{\boldsymbol{\psi}})^2] :, \tag{4}$$

where $\bar{g} \equiv (g_{\uparrow\uparrow} + g_{\uparrow\downarrow})/2$, $\delta g \equiv (g_{\uparrow\uparrow} - g_{\uparrow\downarrow})/2$ and $: \cdots :$ denotes normal order of the field operators.

Lastly, we mention that the total Hamiltonian $\hat{H} = \hat{H}_0 + \hat{H}_{\text{int}}$ can be mapped to one that has the periodicity of the optical lattice potential by means of a unitary transformation [32],

$$U\hat{\boldsymbol{\psi}}(\boldsymbol{r})U^{-1} = \begin{pmatrix} 1 & 0 \\ 0 & e^{-ik_L x - ik_L y} \end{pmatrix}\begin{pmatrix} \hat{\psi}_\uparrow(\boldsymbol{r}) \\ \hat{\psi}_\downarrow(\boldsymbol{r}) \end{pmatrix}. \tag{5}$$

However, we will not adopt such a transformation here.

B. Symmetry

A thorough analysis of the symmetries exhibited by the Hamiltonian is crucial to the understanding of the magnetic phase transition since different phases can be distinguished by, in addition to the order parameter, the specific symmetries that are spontaneously broken. Furthermore, knowledge of these symmetries is rather useful in the calculation of various dynamical response functions of the system, as they ultimately determine the selection rules obeyed by the relevant dynamical transitions between the states. Pertinent to our study are the following three types of symmetries (or symmetry groups): the pseudo $\mathcal{PT}$ symmetry, the modified dihedral $\tilde{D}_4$ symmetry group, and the nonsymmorphic symmetry. In the following, we describe each of these symmetries separately.

Pseudo $\mathcal{PT}$ symmetry. For genuine spin-1/2 particles, the $\mathcal{PT}$ symmetry operation is defined as

$$\mathcal{PT} = i\sigma_y \mathcal{K}\mathcal{I}, \tag{6}$$

where $\mathcal{I}$ is the space inversion operator and $\mathcal{K}$ is the complex conjugation operator. Because the spin in our system is pseudospin, we refer to this as the pseudo $\mathcal{PT}$ symmetry. It is straightforward to show that the single-particle Hamiltonian h_0 in Eq. (2) is indeed invariant under such a transformation, i.e., $(\mathcal{PT})h_0(\mathcal{PT})^{-1} = h_0$, which ensures that $\mathcal{PT}$ commutes with $\hat{H}_0$ in Eq. (1). In addition, it is clear that $\mathcal{PT}$ also commutes with $\hat{H}_{\rm int}$ in Eq. (4) due to the fact that $(\mathcal{PT})\sigma_z(\mathcal{PT})^{-1} = -\sigma_z$.

Modified dihedral symmetry. In the absence of the SO coupling, h_0 has the usual point group D_4 symmetry, which consists of fourfold rotation operations r_n and twofold reflection operations s_n $(n = 1, \ldots, 4)$, as illustrated in Fig. 1(b). Here, r_n denotes the counterclockwise rotation of $n\pi/2$ around the z axis at the origin and s_n denotes the reflection across a line that makes an angle of $n\pi/4$ with the x axis. With SO coupling, however, the Hamiltonian h_0 no longer commutes with these operations because the Raman potentials are not fully invariant under D_4 operations. Instead, as can be easily checked, it commutes with what we will refer to as the modified dihedral symmetry operations,

$$\tilde{r}_n \equiv e^{-i\frac{n\pi}{4}\sigma_z} r_n, \quad \tilde{s}_n \equiv e^{-i\frac{\pi}{2}\vec{s}_n\cdot\vec{\sigma}} s_n, \tag{7}$$

for $n = 1, \ldots, 4$, and

$$\tilde{r}_n \equiv e^{-i\frac{n\pi}{4}\sigma_z} r_{n-4}, \quad \tilde{s}_n \equiv e^{i\frac{\pi}{2}\vec{s}_{n-4}\cdot\vec{\sigma}} s_{n-4}, \tag{8}$$

for $n = 5, \ldots, 8$, where $\vec{s}_n$ is the unit vector along the reflection axis of the s_n operation. These 16 operations form a symmetry group of h_0 denoted by $\tilde{D}_4$, which is a double group of the D_4 point group [33,34]. Again, since each of the operators in $\tilde{D}_4$ either commutes or anticommutes with σ_z, the whole $\tilde{D}_4$ group commutes with $\hat{H}_{\rm int}$.

Nonsymmorphic symmetry. Certain crystal structures are invariant under a combination of point group rotation and nonprimitive lattice translation, which is known as the nonsymmorphic symmetry. An analogous symmetry exists for our system, where the symmetry operations are described by

$$\Lambda_i = T_i(\pi/k_L)e^{-i\frac{\pi}{2}\sigma_z}, \tag{9}$$

where $T_i(l)$ $(i = x, y)$ is a translation along the i direction of a distance l. It can be checked again that such operations commute with $\hat{H}_0$ and $\hat{H}_{\rm int}$. In fact, any combination of Λ_i and a rotation operator in $\tilde{D}_4$ group, i.e.,

$$\Lambda_i R \quad \forall R \in \tilde{D}_4, \tag{10}$$

is also a nonsymmorphic symmetry operation.

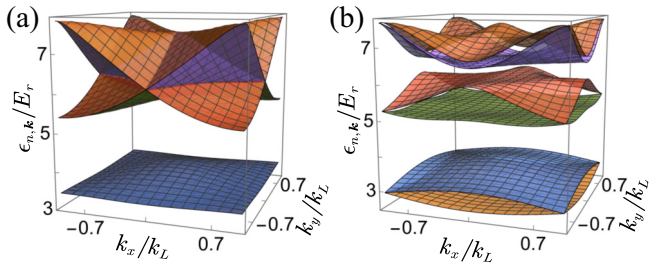

FIG. 2. The first 12 energy bands of the single-particle Hamiltonian: (a) without SO coupling and (b) with SO coupling. The bands are doubly degenerate due to the $\mathcal{PT}$ symmetry. Here, $V_0 = 4E_r$ and $M_0 = 2E_r$, where E_r is the recoil energy. Note that the folded structure of the energy bands for the Hamiltonian without the SO coupling is due to the fact that it is plotted within the first Brillouin zone of the SOC Hamiltonian, which is half the size of that without SO coupling.

III. MAGNETIC PHASE TRANSITION: IN-PLANE VS PERPENDICULAR MAGNETIZATION

As the SO-coupling strength M_0 increases, the condensate in the optical lattice undergoes a phase transition [22] which is analogous to the stripe-to-plane-wave phase transition found in translationally invariant SOC systems [35]. However, since the atoms in our system neither condense at finite crystal momenta nor form density waves, the nomenclature "plane-wave phase" and "stripe phase" are not entirely appropriate here [36]. Instead, we shall see that the phases are characterized by different types of the magnetization, i.e., in-plane vs perpendicular magnetization. In this section, we provide a detailed discussion of this phase transition and reveal important properties of these phases which, upon comparison to those of a recently studied chiral superfluid, suggest that the anomalous Hall effect may exist in this system.

To begin, we first calculate the noninteracting bands of the SOC gas determined by

$$h_0\boldsymbol{\phi}_{n\boldsymbol{k}}(\boldsymbol{r}) = \epsilon_{n\boldsymbol{k}}\boldsymbol{\phi}_{n\boldsymbol{k}}(\boldsymbol{r}), \tag{11}$$

under the periodic boundary condition, where $\epsilon_{n\boldsymbol{k}}$, measured in recoil energy $E_r = \hbar^2 k_L^2/2m$, is the band dispersion and $\boldsymbol{\phi}_{n\boldsymbol{k}}(\boldsymbol{r}) = [\phi_{n\boldsymbol{k}\uparrow}(\boldsymbol{r}), \phi_{n\boldsymbol{k}\downarrow}(\boldsymbol{r})]^T$ is the corresponding two-component Bloch state. Figure 2(b) is an example of the band structure obtained from solving Eq. (11); as a comparison, the band structure in the absence of the SO coupling is shown in Fig. 2(a). An important property of the noninteracting SOC bands is that they are doubly degenerate due to the $\mathcal{PT}$ symmetry, much like the familiar Kramer's degeneracy. This is because $(\mathcal{PT})^2 = -1$ and, as a result, $\mathcal{PT}\boldsymbol{\phi}_{n,\boldsymbol{k}} \neq \boldsymbol{\phi}_{n,\boldsymbol{k}}$. The degeneracy is reflected in Fig. 2(b), which contains the lowest 12 bands. In practice, it is necessary to work with a specific set of single-particle wave functions. This can be obtained

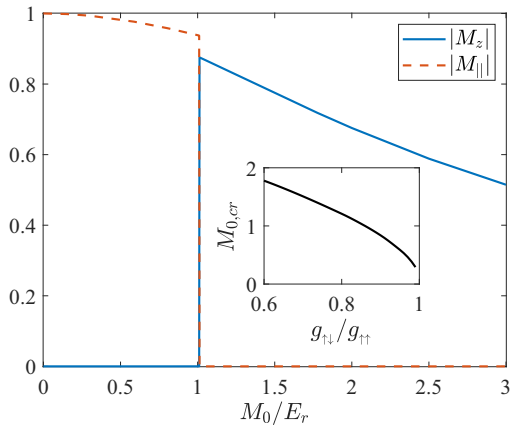

FIG. 3. Magnetization as a function of the SO-coupling strength M_0. Inset: the critical $M_{0,cr}$ as a function of the interaction anisotropy $g_{\uparrow\downarrow}/g_{\uparrow\uparrow}$.

by adding an infinitesimal, $\mathcal{PT}$ symmetry breaking Zeeman energy term $\pm\eta\sigma_z$ to h_0 when solving Eq. (11), where η is a positive infinitesimal number. For concreteness, the states determined by $+\eta\sigma_z$ ($-\eta\sigma_z$) are denoted by $\boldsymbol{\phi}^+_{m,\boldsymbol{k}}$ ($\boldsymbol{\phi}^-_{m,\boldsymbol{k}}$) and are referred to as the spin-up (spin-down) polarized states. As a result of the $\mathcal{PT}$ symmetry, these states are related to each other by $\boldsymbol{\phi}^+_{m,\boldsymbol{k}} = \mathcal{PT}\boldsymbol{\phi}^-_{m,\boldsymbol{k}}$.

For weak atomic interactions and at zero temperature, the atoms naturally condense at $\boldsymbol{k} = 0$ of the Brillouin zone (Γ point); the specific condensate wave function can be determined by minimizing the Gross-Pitaevskii (GP) functional with respect to the trial wave function $\boldsymbol{\psi}(\boldsymbol{r})$ consisting of superpositions of $\boldsymbol{\phi}_{n0}(\boldsymbol{r})$ from different bands. Namely, we minimize the following GP functional:

$$E[\boldsymbol{\psi}] = \int d\boldsymbol{r}\left[\boldsymbol{\psi}^\dagger h_0\boldsymbol{\psi} + \frac{\bar{g}}{2}(\boldsymbol{\psi}^\dagger\boldsymbol{\psi})^2 + \frac{\delta g}{2}(\boldsymbol{\psi}^\dagger\sigma_z\boldsymbol{\psi})^2\right],$$

under the normalization $\int d\boldsymbol{r}\boldsymbol{\psi}^\dagger(\boldsymbol{r})\boldsymbol{\psi}(\boldsymbol{r}) = N$, where N is the total number of atoms. The normalized condensate wave function so obtained will be denoted by $\boldsymbol{\Phi} = (\Phi_\uparrow, \Phi_\downarrow)^T$, for which $\int d\boldsymbol{r}\boldsymbol{\Phi}^\dagger(\boldsymbol{r})\boldsymbol{\Phi}(\boldsymbol{r}) = 1$.

To describe the magnetic properties, we define the magnetization per particle,

$$\boldsymbol{M} = \int d\boldsymbol{r}\,\boldsymbol{m}(\boldsymbol{r}) = \int d\boldsymbol{r}\,\boldsymbol{\Phi}^\dagger(\boldsymbol{r})\boldsymbol{\sigma}\boldsymbol{\Phi}(\boldsymbol{r}), \tag{12}$$

where $\boldsymbol{\sigma} \equiv (\sigma_x, \sigma_y, \sigma_z)$. For weak SO-coupling strengths, the system favors a ground state which minimizes the interaction energy term associated with spin polarization, $\frac{\delta g}{2}\int d\boldsymbol{r}(\boldsymbol{\psi}^\dagger\sigma_z\boldsymbol{\psi})^2$. Recalling that $\delta g = (g_{\uparrow\uparrow} - g_{\uparrow\downarrow})/2 > 0$, we then expect a ground state with $M_z = 0$. As the SO-coupling strength increases, the Raman potential energy may be gradually lowered by the spin flip induced by the SO coupling term; the amount lowered eventually compensates for the increase of the interaction energy, leading to a state with a finite magnetization along the z direction. This picture is indeed confirmed by our calculation. In Fig. 3, we plot the magnitude of $|M_z|$ as a function of the SO coupling strength M_0 for $V_0 = 4E_r$, $\rho g_{\uparrow\uparrow} = 0.35E_r$, and $\rho g_{\uparrow\downarrow} = 0.3E_r$, where $\rho = N/\mathcal{A}$ is the density per unit area. We see that a transition from a phase with a vanishing M_z to that with a finite M_z occurs at a SO-coupling strength $M_{0,cr} \approx E_r$. The critical value of the SO-coupling strength depends significantly on the degree of interaction anisotropy, as shown in the inset of Fig. 3. Interestingly, the former phase is in fact not characterized by a vanishing total magnetization, but rather by a finite in-plane magnetization $|M_\parallel| \equiv \sqrt{M_x^2 + M_y^2}$. In other words, our calculations show a transition from in-plane magnetization to perpendicular magnetization driven by the SO-coupling strength. The properties of these two phases will be examined more closely below.

In the perpendicular magnetization phase, the ground state has a twofold degeneracy as the direction of the magnetization can be either along the $+z$ or the $-z$ direction. For $M_z > 0$, the condensate wave function is given by $\boldsymbol{\Phi} = \sum_m(c^+_m\boldsymbol{\phi}^+_{m0} + c^-_m\boldsymbol{\phi}^-_{m0})$, where the $\boldsymbol{\phi}^+_{m0}$ components are dominant. Clearly, the ground states with opposite M_z are related to each other by the $\mathcal{PT}$ symmetry operation. Let us take a specific value of $M_0 = 2.5E_r$ as an example and consider the case of $M_z > 0$. The spin-up and spin-down components of this condensate wave function are shown in Figs. 4(a)–4(d). The most conspicuous property of the wave function is that the spin-down component contains a significant mixture of the p orbitals of the square optical lattice, which is clearly reflected by the phase winding shown in Fig. 4(d). In fact, the spin-down component forms a vortex lattice with the vortex cores located at the optical lattice sites [see Fig. 4(c)]. The spin-up component, on the other hand, consists of dominantly s orbitals; its phase variation shown in Fig. 4(b) indicate very small mixtures of higher orbitals. A direct implication of the vortex lattice is that the condensate carries a macroscopic angular momentum, which can, in principle, be calculated by

$$L_z = N\sum_\sigma \int d\boldsymbol{r}\Phi^\dagger_\sigma(\boldsymbol{r})(xp_y - yp_x)\Phi_\sigma(\boldsymbol{r}). \tag{13}$$

As is expected, the angular momentum is mostly carried by the spin-down component in this case, which is shown in Fig. 5. The fact that $L_z < 0$ is consistent with the phase winding of the wave function shown in Fig. 4(d).

In addition, from the condensate wave function shown in Figs. 4(a)–4(d), we find that the ground state breaks the $\tilde{D}_4$ symmetry but still retains the $\tilde{C}_4$ symmetry, the latter of which is formed by all the $\tilde{r}_n$ operations. It can be shown that as a consequence, the magnetization density $\boldsymbol{m}(\boldsymbol{r})$ must have the C_4 symmetry and $M_\parallel = 0$, which are confirmed by the calculation shown in Fig. 4(e). Finally, the condensate wave function also preserves the nonsymmorphic symmetry Λ_i and $\Lambda_i R$ for $R \in \tilde{C}_4$. Specifically, we find

$$\Lambda_x\boldsymbol{\Phi} = -i\boldsymbol{\Phi}, \quad \Lambda_y\boldsymbol{\Phi} = -i\boldsymbol{\Phi}. \tag{14}$$

Now we turn to the in-plane magnetization phase, where the condensate wave function is found to be a superposition of $+\eta\sigma_z$ and $-\eta\sigma_z$ states with equal weight, namely, $\boldsymbol{\Phi} = \sum_m(c^+_m\boldsymbol{\phi}^+_{m0} + c^-_m\boldsymbol{\phi}^-_{m0})$ with $|c^+_m| = |c^-_m|$. Our calculations show that there are four degenerate ground states in this phase, characterize by four possible directions of the in-plane magnetization, i.e., along $\pm\vec{s}_1$ and along $\pm\vec{s}_3$. The condensate wave

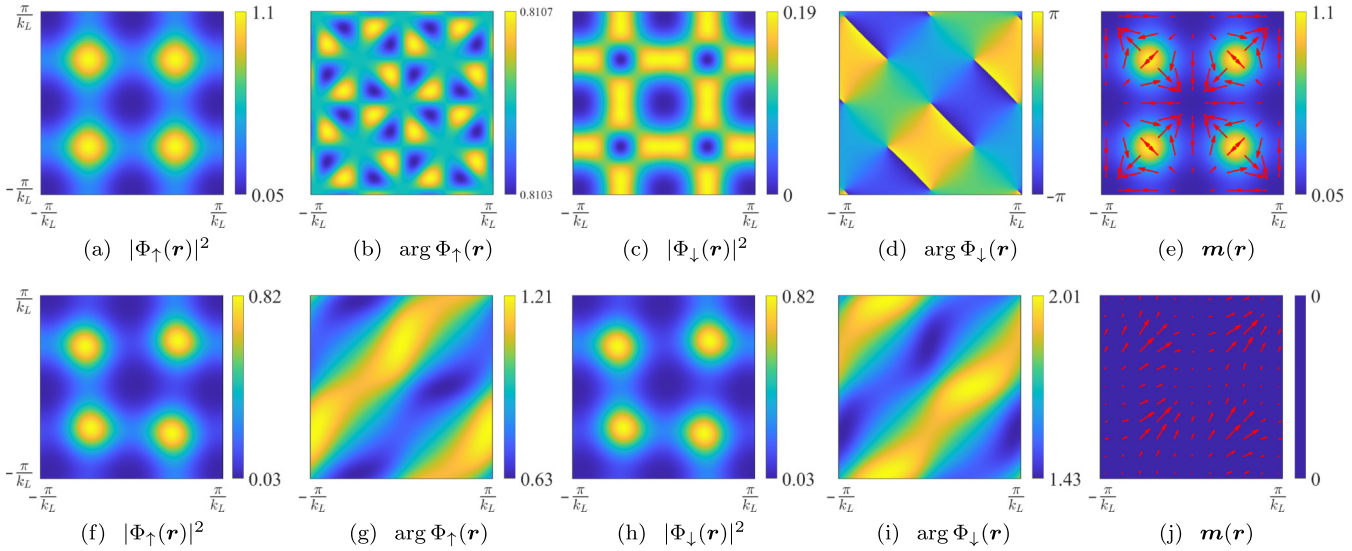

FIG. 4. Condensate wave function $\boldsymbol{\Phi}(\boldsymbol{r})$ (normalized within the Wigner-Seitz cell) and magnetization density $\boldsymbol{m}(\boldsymbol{r})$. Upper panels: perpendicular magnetization phase with SO-coupling strength $M_0 = 2.5E_r$. Lower panels: in-plane magnetization phase with SO-coupling strength $M_0 = 0.8E_r$. Other parameters are $V_0 = 4E_r$, $\rho g_{\uparrow\uparrow} = 0.35E_r$, and $\rho g_{\uparrow\downarrow} = 0.3E_r$. These values will be used in the calculations throughout the paper, unless indicated otherwise.

function for these states can be distinguished by the relative phase of the dominant coefficients c_1^+ and c_1^-, which assume values of $(2q-1)\pi/4$, with $q = 1, 2, 3, 4$. As a specific example, the condensate wave function corresponding to $q = 1$ is shown in Figs. 4(f)–4(i). From these results, we find that wave function is invariant under the symmetry group $\tilde{D}_1 = \{e = \tilde{r}_8, \tilde{s}_1, \tilde{s}_1^2 = \tilde{r}_4, \tilde{s}_1^3 = \tilde{s}_5\}$. Indeed, it can be confirmed that the wave function satisfies

$$\tilde{s}_1\boldsymbol{\Phi} = -i\boldsymbol{\Phi}. \tag{15}$$

This allows us to show that the direction of the magnetization is along the $\vec{s}_1$ axis, as can be seen in Fig. 4(j). In addition, because

$$\tilde{s}_1\hat{L}_z\tilde{s}_1^{-1} = -\hat{L}_z, \tag{16}$$

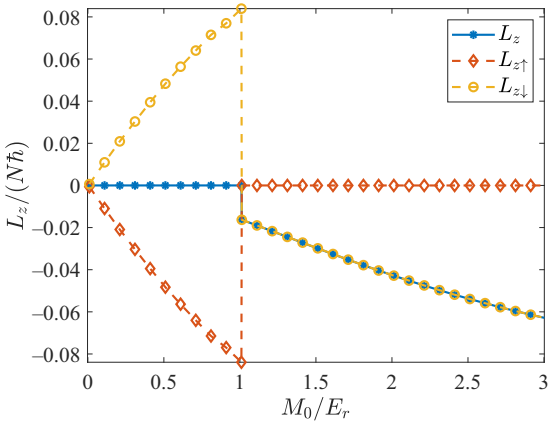

FIG. 5. Angular momentum of the SOC condensate as a function of the SO-coupling strength M_0. Here, the center of the Wigner-Seitz cell is chosen as the origin in the calculation.

where $\hat{L}_z = \sum_\sigma \int d\boldsymbol{r}\hat{\psi}_\sigma^\dagger(\boldsymbol{r})(xp_y - yp_x)\hat{\psi}_\sigma(\boldsymbol{r})$, the total angular momentum of the state vanishes due to this symmetry. This is also confirmed by the calculations shown in Fig. 5, where we see that the up and down component carries opposite angular momentum. Lastly, the condensate wave function preserves the nonsymmorphic symmetries $\Lambda_i\tilde{r}_2$ and $\Lambda_i\tilde{r}_2R$ for $R \in \tilde{D}_1$, as can be easily checked that

$$\Lambda_x\tilde{r}_2\boldsymbol{\Phi} = -\boldsymbol{\Phi}, \quad \Lambda_y\tilde{r}_2\boldsymbol{\Phi} = -\boldsymbol{\Phi}. \tag{17}$$

IV. FINITE-FREQUENCY ANOMALOUS HALL EFFECT

Previous calculations of the ground-state properties reveal that in the perpendicular magnetization phase, the SOC gas contains a vortex lattice in one of the spin components and, consequently, carries a global angular momentum. This is reminiscent of the bosonic chiral superfluid in the boron nitride lattice where an intrinsic AHE was predicted recently [30]. Motivated by this observation, we now explore the prospects of the anomalous Hall effect in the SOC system and calculate the frequency-dependent Hall conductivity by means of the Kubo formula and the Bogoliubov theory. First, we make use of the spectral representation of the Kubo formula, which expresses the Hall conductivity in terms of the energies of the collective excitations and the transition matrix elements of the current operator. These latter quantities are then calculated using the Bogoliubov theory, aided by group symmetry analysis. We find that the current matrix elements obey certain selection rules determined by the symmetry properties of the Bogoliubov Hamiltonian, which in turn are dependent on those of the condensate wave function. These selection rules can be used to understand the overall structure of the frequency-dependent Hall conductivity and to explain the existence of the dc AHE in the perpendicular magnetization phase and the absence of it in the in-plane magnetization phase.

A. Hall conductivity: Spectral representation

The Kubo formula for the Hall conductivity is

$$\sigma_H(\omega) \equiv -\frac{i}{\mathcal{A}\omega}\chi^J_{x,y}(\omega), \tag{18}$$

where $\mathcal{A}$ is the system's area, $\chi^O_{x,y}(\omega)$ is the Fourier transform of the retarded correlation function of operator $\hat{\boldsymbol{O}}$,

$$\chi^O_{x,y}(t-t') = -i\hbar^{-1}\theta(t-t')\langle[\hat{O}_x(t), \hat{O}_y(t')]\rangle, \tag{19}$$

and the total current operator is

$$\hat{\boldsymbol{J}} = \frac{\hbar}{mi}\sum_\sigma \int d\boldsymbol{r}\hat{\psi}^\dagger_\sigma(\boldsymbol{r})\nabla\hat{\psi}_\sigma(\boldsymbol{r}). \tag{20}$$

Quite generally, the Hall conductivity can be written in a form of spectral representation as

$$\sigma_H(\omega) = -i\frac{1}{\mathcal{A}\omega\hbar^2}\sum_{n\neq 0}\left[\frac{J_{x,0n}J_{y,n0}}{\hbar\omega - E_n + E_0 + i0^+} - \frac{J_{y,0n}J_{x,n0}}{\hbar\omega + E_n - E_0 + i0^+}\right], \tag{21}$$

where E_n denotes the energy of the many-body eigenstate $|n\rangle$ and $J_{i,0n} = \langle 0|\hat{J}_i|n\rangle$ denotes the current matrix element between the ground state and the excited state $|n\rangle$.

As can be seen in Eq. (21), the Hall conductivity is a complex quantity; its real and imaginary parts are related to each other by the Kramer-Kronig relation,

$$\mathrm{Re}\sigma_H(\omega) = \frac{1}{\pi}\mathcal{P}\int_{-\infty}^{\infty} d\omega' \frac{\mathrm{Im}\sigma_H(\omega')}{\omega' - \omega}. \tag{22}$$

Writing the matrix product $J_{x,0n}J_{y,n0}$ in terms of its real and imaginary part as

$$J_{x,0n}J_{y,n0} = I_n + iI'_n, \tag{23}$$

where I_n and I'_n are now real, we can explicitly obtain the real and imaginary parts as

$$\mathrm{Re}\,\sigma_H(\omega) = \frac{1}{\mathcal{A}\omega\hbar^2}\sum_{n\neq 0}\left\{\frac{2\hbar\omega}{(\hbar\omega)^2 - (E_n - E_0)^2}I'_n + \pi[\delta(\hbar\omega + E_n - E_0) - \delta(\hbar\omega - E_n + E_0)]I_n\right\} \tag{24}$$

and

$$\mathrm{Im}\,\sigma_H(\omega) = -\frac{1}{\mathcal{A}\omega\hbar^2}\sum_{n\neq 0}\left\{\frac{2(E_n - E_0)}{(\hbar\omega)^2 - (E_n - E_0)^2}I_n + \pi[\delta(\hbar\omega + E_n - E_0) + \delta(\hbar\omega - E_n + E_0)]I'_n\right\}. \tag{25}$$

Later we shall see that the symmetry of the Hamiltonian places various constraints on the current matrix elements. For the purpose of such symmetry analysis, it is useful to write the real and imaginary parts of the matrix elements product in Eq. (23) in slightly different forms. Introducing the operators

$$\hat{J}_\pm = \tfrac{1}{2}(\hat{J}_x \pm i\hat{J}_y), \tag{26}$$

we arrive at

$$I_n = -i(J_{+,0n}J_{+,n0} - \text{c.c.}), \tag{27}$$

$$I'_n = -(|J_{+,n0}|^2 - |J_{-,n0}|^2), \tag{28}$$

where $J_{\pm,nm} \equiv \langle n|\hat{J}_\pm|m\rangle$. We note that the dc conductivity, defined by $\mathrm{Re}\,\sigma_H(0)$, is given by

$$\mathrm{Re}\,\sigma_H(0) = -\frac{2}{\mathcal{A}\hbar}\sum_{n\neq 0}\frac{I'_n}{(E_n - E_0)^2}. \tag{29}$$

B. Bogoliubov theory

For the SOC condensate, the above matrix elements will be evaluated using the Bogoliubov approximation, under which the current operator is given by

$$\hat{\boldsymbol{J}} \approx \frac{\hbar\sqrt{N}}{mi}\sum_\sigma\int d\boldsymbol{r}[\Phi^*_\sigma\nabla\delta\hat{\psi}_\sigma - \Phi_\sigma\nabla\delta\hat{\psi}^\dagger_\sigma]. \tag{30}$$

Here the fluctuation operator $\delta\hat{\psi}_\sigma$ can be expressed as

$$\delta\hat{\psi}_\sigma(\boldsymbol{r}) = \sum_{n\boldsymbol{k}} u_{n\boldsymbol{k}\sigma}(\boldsymbol{r})\hat{\alpha}_{n\boldsymbol{k}} - v^*_{n\boldsymbol{k}\sigma}(\boldsymbol{r})\hat{\alpha}^\dagger_{n\boldsymbol{k}}, \tag{31}$$

where $n = 0, 1, 2\ldots$ is now the band index (to be distinguished from that used previously to denote a general excited state), $\hat{\alpha}^\dagger_{n\boldsymbol{k}}$ is the creation operator for the Bogoliubov quasiparticle, and $u_{n\boldsymbol{k}\sigma}$ and $v_{n\boldsymbol{k}\sigma}$ are the Bogoliubov amplitudes. These amplitudes are determined by the Bogoliubov–de Gennes (BdG) equation,

$$\tau_z\mathcal{H}_B(\boldsymbol{r})\boldsymbol{V}_{n\boldsymbol{k}}(\boldsymbol{r}) = \mathcal{E}_{n\boldsymbol{k}}\boldsymbol{V}_{n\boldsymbol{k}}(\boldsymbol{r}), \tag{32}$$

where $\tau_z = \sigma_z \otimes I$, $\mathcal{E}_{n\boldsymbol{k}}$ is the band dispersion of the quasiparticle, $\boldsymbol{V}_{n\boldsymbol{k}} \equiv (\boldsymbol{u}^T_{n\boldsymbol{k}}, -\boldsymbol{v}^T_{n\boldsymbol{k}})^T$ is the corresponding amplitude with the normalization $\int d\boldsymbol{r}\boldsymbol{V}^\dagger_{m\boldsymbol{k}}(\boldsymbol{r})\tau_z\boldsymbol{V}_{n\boldsymbol{k}}(\boldsymbol{r}) = \tau_{z,mn}$, and $\mathcal{H}_B(\boldsymbol{r})$ is the Bogoliubov Hamiltonian,

$$\mathcal{H}_B(\boldsymbol{r}) = \begin{pmatrix}\mathcal{M} + h_0 - \mu & \mathcal{N} \\ \mathcal{N}^* & \mathcal{M}^* + h_0^* - \mu\end{pmatrix}. \tag{33}$$

Here, μ is the chemical potential determined earlier along with the condensate wave function $\boldsymbol{\Phi}$,

$$\mathcal{M} = \rho\mathcal{A}\begin{pmatrix}2g_{\uparrow\uparrow}|\Phi_\uparrow|^2 + g_{\uparrow\downarrow}|\Phi_\downarrow|^2 & g_{\uparrow\downarrow}\Phi^*_\downarrow\Phi_\uparrow \\ g_{\uparrow\downarrow}\Phi^*_\uparrow\Phi_\downarrow & 2g_{\downarrow\downarrow}|\Phi_\downarrow|^2 + g_{\uparrow\downarrow}|\Phi_\uparrow|^2\end{pmatrix}$$

and

$$\mathcal{N} = \rho\mathcal{A}\begin{pmatrix}g_{\uparrow\uparrow}\Phi^2_\uparrow & g_{\uparrow\downarrow}\Phi_\downarrow\Phi_\uparrow \\ g_{\uparrow\downarrow}\Phi_\uparrow\Phi_\downarrow & g_{\downarrow\downarrow}\Phi^2_\downarrow\end{pmatrix}.$$

Examples of the Bogoliubov quasiparticle spectrum obtained by solving Eq. (32) in the perpendicular and in-plane magnetization phases are shown in Fig. 6 and Fig. 9, respectively. We note that there is a gapless solution to the BdG equation in both phases as a result of the well-known Goldstone theorem. The corresponding eigenvector, for which $n = 0$ and $\boldsymbol{k} = 0$, reproduces the GP wave function and takes the form of $\boldsymbol{V}_{00} = (\boldsymbol{\Phi}^T, -\boldsymbol{\Phi}^\dagger)^T$.

Since the total current conserves the crystal momentum, the relevant current matrix elements within the Bogoliubov theory are those between the ground state and the excited states with one quasiparticle of zero crystal momentum. Using

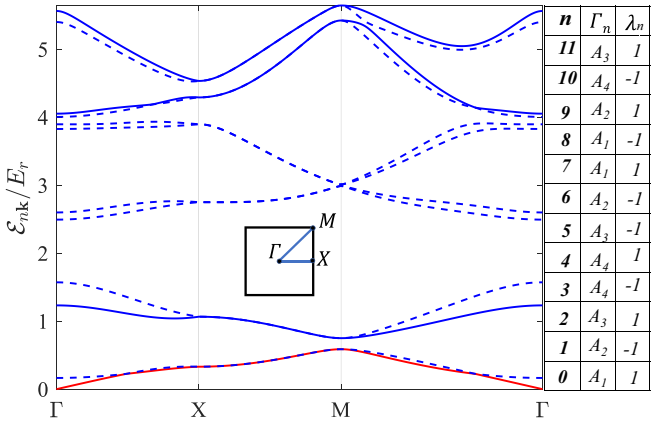

FIG. 6. Bogoliubov bands in the perpendicular magnetization phase. On the right side, the Γ_n and the λ_n value corresponding to the $\boldsymbol{k} = 0$ state of the nth band are given. According to the selection rule explained in the text, the transition is forbidden from the ground state to those bands indicated by dashed lines.

Eqs. (30) and (31), we find that the matrix elements $J_{\pm,n0}$ are given by

$$J_{\pm,n0} = \frac{\hbar\sqrt{N}}{mi}\sum_{\sigma}\int d\boldsymbol{r}(u^*_{n0\sigma}\partial_{\pm}\Phi_{\sigma} + v^*_{n0\sigma}\partial_{\pm}\Phi^*_{\sigma})$$
$$\equiv \sqrt{N}\langle \boldsymbol{V}_{n0}|\mathcal{J}_{\pm}|\boldsymbol{V}_{00}\rangle, \tag{34}$$

where

$$\mathcal{J}_{\pm} \equiv (\hbar/mi)\mathrm{diag}(\partial_{\pm}, \partial_{\pm}, \partial_{\pm}, \partial_{\pm}), \tag{35}$$

with $\partial_{\pm} \equiv (\partial_x \pm i\partial_y)/2$. Although it is straightforward to calculate Eq. (34) using the solutions from the Bogoliubov equation, such a task can be greatly simplified if we make use of the symmetry properties of the Bogoliubov Hamiltonian and its eigenstates. First, it can be shown by such symmetry analysis that the matrix elements product $J_{x,0n}J_{y,n0}$ in Eq. (23) is purely imaginary in the perpendicular magnetization phase and purely real in the in-plane magnetization phase. This property alone indicates that the dc AHE is absent in the latter phase. Furthermore, these matrix elements obey selection rules governed by the symmetry group of the Bogoliubov Hamiltonian; these selection rules determine the overall structure of the complex Hall conductivity.

In order to demonstrate the above properties, we first discuss the symmetry of the Bogoliubov Hamiltonian, which crucially depends on that of the condensate wave function $\boldsymbol{\Phi}$. We found earlier that even though $\boldsymbol{\Phi}$ breaks the $\tilde{D}_4$ symmetry, it nevertheless preserves a symmetry subgroup of $\tilde{D}_4$. Suppose that $\boldsymbol{\Phi}$ is invariant under a symmetry operation $R \in \tilde{D}_4$, i.e.,

$$R\boldsymbol{\Phi} = e^{i\theta_R}\boldsymbol{\Phi}. \tag{36}$$

Then, it is straightforward to show that

$$f_1(R) = \begin{pmatrix} e^{-i\theta_R}R & \\ & \mathcal{K}e^{-i\theta_R}R\mathcal{K} \end{pmatrix} \tag{37}$$

is a symmetry operator of $\mathcal{H}_B$, namely,

$$f_1(R)\mathcal{H}_B f_1^{-1}(R) = \mathcal{H}_B. \tag{38}$$

TABLE I. Character table of $\tilde{C}_4$.

$\tilde{C}_4$	e	$\tilde{r}_1$	$\tilde{r}_2$	$\tilde{r}_3$	$\tilde{r}_4$	$\tilde{r}_5$	$\tilde{r}_6$	$\tilde{r}_7$
A_1	1	1	1	1	1	1	1	1
A_2	1	i	-1	$-i$	1	i	-1	i
A_3	1	$-i$	-1	i	1	$-i$	-1	i
A_4	1	-1	1	-1	1	-1	1	-1
A_5	1	$e^{-i\pi/4}$	$e^{-i\pi/2}$	$e^{-i3\pi/4}$	$e^{-i\pi}$	$e^{i3\pi/4}$	$e^{i\pi/2}$	$e^{i\pi/4}$

In addition, the condensate wave function may also retain certain nonsymmorphic symmetry $\Lambda_i R$. In this case, we have

$$(\Lambda_i R)\boldsymbol{\Phi} = e^{i\beta_{i,R}}\boldsymbol{\Phi}, \tag{39}$$

which allows us to similarly define a corresponding symmetry operation for $\mathcal{H}_B$ as

$$f_2(\Lambda_i R) = \begin{pmatrix} e^{-i\beta_{i,R}}\Lambda_i R & \\ & \mathcal{K}e^{-i\beta_{i,R}}\Lambda_i R\mathcal{K} \end{pmatrix}. \tag{40}$$

In the following, we will discuss in detail the implications of these symmetry operators for $\mathcal{H}_B$. To do so, we need to treat the two magnetic phases separately because their corresponding condensate wave functions possess different symmetry subgroups of $\tilde{D}_4$ and also different nonsymmorphic symmetries.

C. Perpendicular magnetization phase

As previously found, the condensate wave function $\boldsymbol{\Phi}$ in the perpendicular magnetization phase preserves the $\tilde{C}_4$ symmetry. In Table I, we display the character table of relevant 1D irreducible representations of the $\tilde{C}_4$ group. We again take the case of $M_z > 0$ as an example, where our calculation shows that $\boldsymbol{\Phi}$ is the basis function of the 1D irreducible representation A_5 of the $\tilde{C}_4$ group. Thus, from Eq. (36), we have

$$e^{i\theta_R} = \chi^{(A_5)}(R), \tag{41}$$

where $\chi^{(\Gamma)}(R)$ denotes the character of R in the 1D representation Γ of $\tilde{C}_4$. With this phase factor so determined, it is straightforward to show from Eq. (37) that $f_1(R)\cdot f_1(R') = f_1(R\cdot R')$ for arbitrary $R, R' \in \tilde{C}_4$. This means that all the $f_1(R)$ operations for $R \in \tilde{C}_4$ form a symmetry group of $\mathcal{H}_B$ isomorphic to $\tilde{C}_4$, which we denote as $\tilde{\mathcal{C}}_4 \equiv \{f_1(R) : \forall R \in \tilde{C}_4\}$. Since the solutions of the BdG equation are nondegenerate, the existence of this symmetry group implies that $\boldsymbol{V}_{n0}$ is the basis function of some 1D irreducible representation of $\tilde{C}_4$, denoted by Γ_n. Each of Γ_n can be found by calculating $f_1(R)\boldsymbol{V}_{n0}$ and comparing the result to the character table in Table I. For example, it is easy to show that Γ_0 is the trivial representation A_1. In addition, by direct calculations of $f_1(R)\mathcal{J}_{\pm}f_1^{-1}(R)$, we find that the operators $\mathcal{J}_{\pm}$ are also basis functions of certain 1D irreducible representations of $\tilde{C}_4$, denoted by $\Gamma_{\pm}$. Comparing these calculations to the character table of the 1D representations of $\tilde{C}_4$ in Table I, we find that $\Gamma_+ = A_2$ and $\Gamma_- = A_3$.

Now, we are in a position to discuss the selection rule of the matrix element $\langle \boldsymbol{V}_{n0}|\mathcal{J}_+|\boldsymbol{V}_{00}\rangle$ required by the $\tilde{\mathcal{C}}_4$ symmetry group. The matrix element should transform as a constant when any symmetry group operation is applied to the states

and the operator $\mathcal{J}_+$ simultaneously; otherwise, it must be zero. In the language of group theory [34], this is saying that such a matrix element must vanish if

$$\Gamma_n \neq \Gamma_0 \otimes \Gamma_+. \tag{42}$$

Similarly, we have $\langle \boldsymbol{V}_{n0}|\mathcal{J}_-|\boldsymbol{V}_{00}\rangle = 0$ if

$$\Gamma_n \neq \Gamma_0 \otimes \Gamma_-. \tag{43}$$

The first consequence of this selection rule is that the general expressions of the Hall conductivity in Eqs. (24) and (25) can be immediately simplified. Applying the rule to the matrix elements product $\langle \boldsymbol{V}_{00}|\mathcal{J}_+|\boldsymbol{V}_{n0}\rangle\langle \boldsymbol{V}_{n0}|\mathcal{J}_+|\boldsymbol{V}_{00}\rangle = (\langle \boldsymbol{V}_{n0}|\mathcal{J}_-|\boldsymbol{V}_{00}\rangle)^*\langle \boldsymbol{V}_{n0}|\mathcal{J}_+|\boldsymbol{V}_{00}\rangle$, we see that it must vanish due to the fact that $\Gamma_+ \neq \Gamma_-$. In view of Eqs. (34) and (27), this immediately leads to $I_n = 0$. Consequently, within the Bogoliubov theory, the Hall conductivity takes the form of

$$\mathrm{Re}\,\sigma_H(\omega) = \frac{2}{\mathcal{A}\hbar}\sum_{n\neq 0}\frac{I_n'}{(\hbar\omega)^2 - (\mathcal{E}_{n0} - \mathcal{E}_{00})^2} \tag{44}$$

and

$$\mathrm{Im}\,\sigma_H(\omega) = -\frac{\pi}{\mathcal{A}\omega\hbar^2} \times \sum_{n\neq 0}[\delta(\hbar\omega + \mathcal{E}_{n0} - \mathcal{E}_{00}) + \delta(\hbar\omega - \mathcal{E}_{n0} + \mathcal{E}_{00})]I_n', \tag{45}$$

where the Bogoliubov quasiparticle energy $\mathcal{E}_{n0}$ is determined from the BdG equation and

$$I_n' = -N(|\langle \boldsymbol{V}_{n0}|\mathcal{J}_+|\boldsymbol{V}_{00}\rangle|^2 - |\langle \boldsymbol{V}_{n0}|\mathcal{J}_-|\boldsymbol{V}_{00}\rangle|^2). \tag{46}$$

We note that the real part of the complex Hall conductivity is reactive, while the imaginary part is absorptive, the same as those found in condensed matter systems. The quantity I_n' is not finite for all n due to the selection rule; it vanishes for those states whose corresponding 1D $\tilde{\mathcal{C}}_4$ group representation satisfies both Eqs. (42) and (43). In other words, the selection rule of the $\tilde{\mathcal{C}}_4$ symmetry allows only transitions to states whose 1D $\tilde{\mathcal{C}}_4$ group representation is either A_2 or A_3. In addition, the nonsymmorphic symmetry imposes further restrictions among these states. Because the condensate wave function satisfies the nonsymmorphic symmetry Λ_x, a corresponding symmetry operation, $f_2(\Lambda_x)$ defined by Eq. (40), exists for the Bogoliubov Hamiltonian. Under this operation, $\mathcal{J}_\pm$ and the Bogoliubov amplitude $\boldsymbol{V}_{n0}$ transform as

$$f_2(\Lambda_x)\mathcal{J}_\pm f_2^{-1}(\Lambda_x) = \mathcal{J}_\pm, \quad f_2(\Lambda_x)\boldsymbol{V}_{n0} = \lambda_n \boldsymbol{V}_{n0}. \tag{47}$$

This means that transitions to those states for which $\lambda_n \neq \lambda_0$ are forbidden by the nonsymmorphic symmetry. In Fig. 6, we show a table of calculated Γ_n and λ_n for the first 12 bands. As can be checked from this table, the combination of the two sets of selection rules limits the relevant excited bands to $n = 2, 9, 11$.

In Fig. 7, we have shown an example of $\mathrm{Re}\,\sigma_H(\omega)$, where we find resonances located precisely at the Γ point excitation energies of these bands. The imaginary part $\mathrm{Im}\,\sigma_{\mathrm{H}}(\omega)$, shown in Fig. 8, is given by the summation of a series of δ functions centered at these excitation energies, with weights determined by the corresponding I_n'. Notably, our calculations show a finite dc Hall conductivity $\mathrm{Re}\,\sigma_H(0)$ for the perpendicular magnetization phase, which is in sharp contrast with the in-plane magnetization phase to be discussed below. We will return to the issue of dc Hall conductivity later in Sec. V.

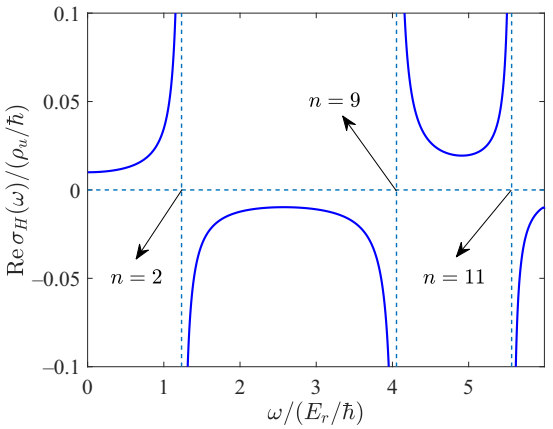

FIG. 7. Real part of the frequency-dependent Hall conductivity for the system in the perpendicular magnetization phase. The specific excitation bands corresponding to the resonances are indicated by the arrows. Here, ρ_u is the number of atoms per unit cell.

D. In-plane magnetization phase

In comparison to the perpendicular magnetization phase, the condensate wave function in the in-plane magnetization phase preserves the $\tilde{D}_1$ symmetry. To be specific, we take the condensate wave function considered in Sec. III as an example. Our calculation shows that this condensate wave function is the basis function of the 1D irreducible representation B_4 of the $\tilde{D}_1$ group (see the character table of the representations of the $\tilde{D}_1$ in Table II). Letting

$$e^{i\theta_R} = \chi^{(B4)}(R), \tag{48}$$

we can again form a symmetry group of $\mathcal{H}_B$, $\tilde{\mathcal{D}}_1 \equiv \{f_1(R) : \forall R \in \tilde{D}_1\}$, which is isomorphic to $\tilde{D}_1$. We now show that $I_n' = 0$ as a result of this symmetry. It can be easily checked

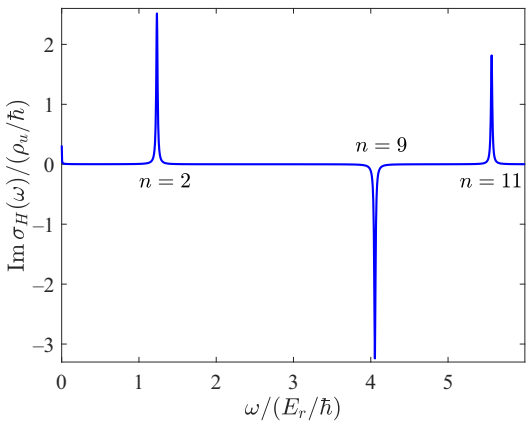

FIG. 8. Imaginary part of the frequency-dependent Hall conductivity for the system in the perpendicular magnetization phase. Here the δ peaks are broadened using a Lorentzian with a width parameter 0.01.

TABLE II. Character table of $\tilde{D}_1$.

$\tilde{D}_1$	e	$\tilde{s}_1$	$\tilde{s}_1^2$	$\tilde{s}_1^3$
B_1	1	1	1	1
B_2	1	−1	1	−1
B_3	1	i	−1	−i
B_4	1	−i	−1	i
E	2	0	2	0

that for $\tilde{s}_1 \in \tilde{D}_1$,

$$f_1(\tilde{s}_1)\mathcal{J}_+ f_1^{-1}(\tilde{s}_1) = i\mathcal{J}_-. \tag{49}$$

Indeed, it turns out that $\mathcal{J}_+$ and $\mathcal{J}_-$ are the basis functions of a 2D representation of $\tilde{\mathcal{D}}_1$ group, denoted here by $\Gamma_{\mathcal{J}}$. The above transformation, together with the fact that $\boldsymbol{V}_{n0}$ is the basis function of a 1D representation of the $\tilde{\mathcal{D}}_1$ group, leads to

$$|\langle \boldsymbol{V}_{n0}|\mathcal{J}_+|\boldsymbol{V}_{00}\rangle| = |\langle \boldsymbol{V}_{n0}|\mathcal{J}_-|\boldsymbol{V}_{00}\rangle|. \tag{50}$$

In view of Eqs. (34) and (27), we then arrive at $I_n' = 0$ and

$$\mathrm{Re}\,\sigma_H(\omega) = \frac{\pi}{\mathcal{A}\omega\hbar^2}\sum_{n\neq 0}[\delta(\hbar\omega + \mathcal{E}_{n0} - \mathcal{E}_{00}) - \delta(\hbar\omega - \mathcal{E}_{n0} + \mathcal{E}_{00})]I_n, \tag{51}$$

$$\mathrm{Im}\,\sigma_H(\omega) = -\frac{1}{\mathcal{A}\omega\hbar^2}\sum_{n\neq 0}\frac{2(\mathcal{E}_{n0} - \mathcal{E}_{00})}{(\hbar\omega)^2 - (\mathcal{E}_{n0} - \mathcal{E}_{00})^2}I_n, \tag{52}$$

where

$$I_n = -iN(\langle \boldsymbol{V}_{00}|\mathcal{J}_+|\boldsymbol{V}_{n0}\rangle\langle \boldsymbol{V}_{n0}|\mathcal{J}_+|\boldsymbol{V}_{00}\rangle - \mathrm{c.c.}). \tag{53}$$

Interestingly, the form of the complex Hall conductivity here is drastically different from that in the perpendicular magnetization phase, in that the real part is absorptive whereas the imaginary part is reactive. In particular, the dc Hall conductivity $\mathrm{Re}\,\sigma_H(0)$ vanishes completely.

Similar to previous analysis of the perpendicular magnetization phase, we can determine the selection rules of the matrix elements $\langle \boldsymbol{V}_{00}|\mathcal{J}_\pm|\boldsymbol{V}_{n0}\rangle$ by first ascertaining the representations of the $\tilde{D}_1$ group whose basis functions correspond to $\boldsymbol{V}_{00}$, $\boldsymbol{V}_{n0}$, and $\mathcal{J}_\pm$. For operators $\mathcal{J}_\pm$ that construct a higher than 1D representation, the generalization of the selection rule given earlier states that the matrix elements $\langle \boldsymbol{V}_{00}|\mathcal{J}_\pm|\boldsymbol{V}_{n0}\rangle$ vanish if Γ_n is not contained in the 1D decomposition of the direct product $\Gamma_{\mathcal{J}} \otimes \Gamma_0$ [34]. From direct calculation and the character table, we find that $\Gamma_{\mathcal{J}} = E$ and thus

$$\Gamma_{\mathcal{J}} \otimes \Gamma_0 = B_1 \oplus B_2. \tag{54}$$

As shown in Fig. 9, it turns out that Γ_n is in fact either B_1 or B_2 for the first 11 excited bands, meaning that for these bands no restriction of transition is placed by this rule. However, this is not the case with respect to the selection rule of the nonsymmorphic symmetry. Recalling that the condensate here is invariant under $\Lambda_x\tilde{r}_2$, we can define the corresponding symmetry operation $f_2(\Lambda_x\tilde{r}_2)$ for the Bogoliubov Hamiltonian. Considering I_n under the following transformations:

$$f_2(\Lambda_x\tilde{r}_2)\mathcal{J}_\pm f_2^{-1}(\Lambda_x\tilde{r}_2) = -\mathcal{J}_\pm, \qquad f_2(\Lambda_x\tilde{r}_2)\boldsymbol{V}_{n0} = \lambda_n'\boldsymbol{V}_{n0}, \tag{55}$$

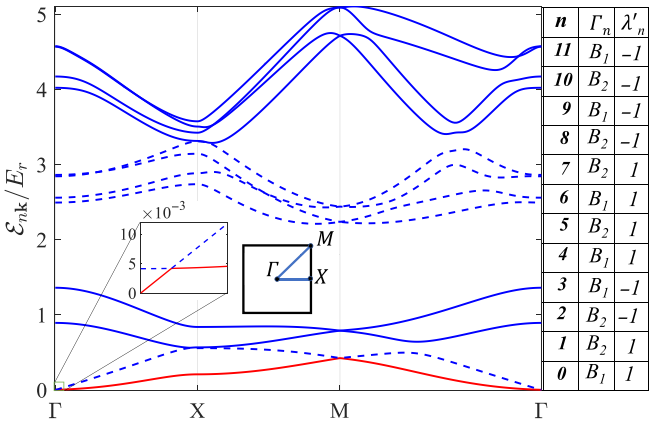

n	Γ_n	λ_n'
11	B_1	-1
10	B_2	-1
9	B_1	-1
8	B_2	-1
7	B_2	1
6	B_1	1
5	B_2	1
4	B_1	1
3	B_1	-1
2	B_2	-1
1	B_2	1
0	B_1	1

FIG. 9. Bogoliubov bands in the in-plane magnetization phase. Although it appears that this phase has two gapless modes, the expanded view of the neighborhood of the Γ point shows that this is not the case. On the right side, the Γ_n and the λ value corresponding to the $\boldsymbol{k} = 0$ state of the nth band are given. According to the selection rule explained in the text, the transition is forbidden from the ground state to those bands indicated by dashed lines.

it is not difficult to see that $I_n \neq 0$ only if $\lambda_n' = -\lambda_0'$. According to the table of λ_n' values shown in Fig. 9, this rule then eliminates transitions to those states from the bands indicated by dashed lines. Again, this is consistent with the detailed calculations of $\mathrm{Im}\,\sigma_{\mathrm{H}}(\omega)$ and $\mathrm{Re}\,\sigma_{\mathrm{H}}(\omega)$, shown in Figs. 10 and 11, respectively.

V. DC HALL CONDUCTIVITY

In the previous section, we have demonstrated the existence of the anomalous Hall effect by explicit calculations of the frequency-dependent Hall conductivity. We found that the current transition matrix elements obey certain selection rules dictated by symmetry principals, which are used to explain the various resonances exhibited in the frequency-dependent Hall conductivities as well as the absence of the dc Hall conductivity in the in-plane magnetization phase. However,

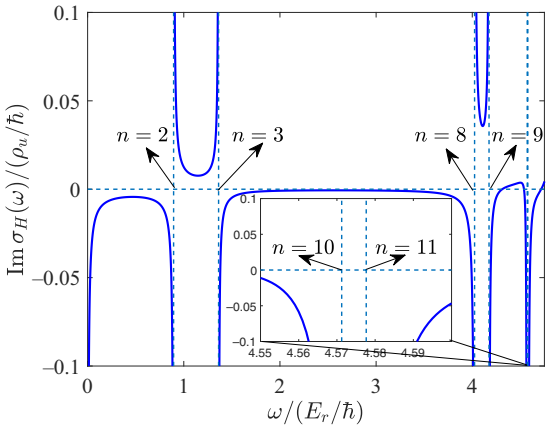

FIG. 10. Imaginary part of the frequency-dependent Hall conductivity for the system in the in-plane magnetization phase. The specific excitation bands corresponding to the resonances are indicated by the arrows.

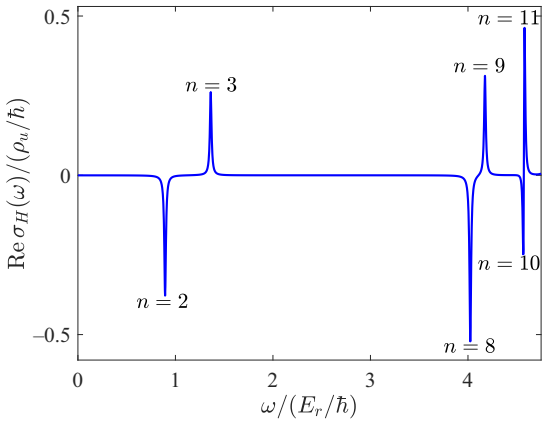

FIG. 11. Real part of the frequency-dependent Hall conductivity for the system in the in-plane magnetization phase. Here the δ peaks are broadened using a Lorentzian with a width parameter 0.01.

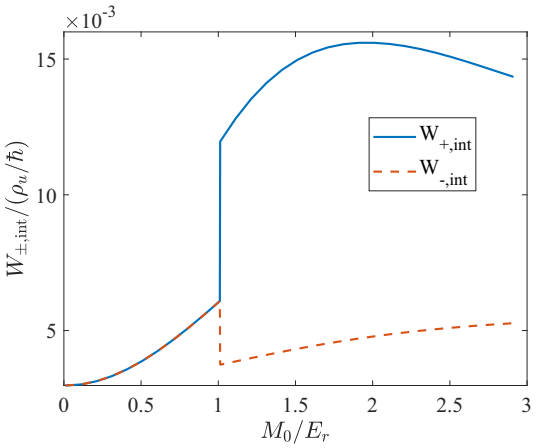

FIG. 12. Integrated excitation rates $W_{\pm,\mathrm{int}}$ due to the rotating potentials in Eq. (56), as a function of the SO-coupling strength.

these calculations do not provide underlying reasons for why the dc AHE is present in one phase but not in the other. In this section, we focus on the dc Hall conductivity and explore, from both a real- and momentum-space perspective, a deeper understanding of the causes of the AHE in the atomic superfluid. From the real-space perspective, we argue that the chirality of the superfluid is directly responsible for a finite dc Hall conductivity; from the momentum-space perspective, we show that finite Berry curvature at the condensation momentum of the noninteracting band underpins the dc Hall conductivity.

A. Real-space perspective: Chirality

In addition to the magnetization, chirality is another fundamental property that distinguishes the two magnetic phases. In contrast to the in-plane magnetization phase, the condensate in the perpendicular magnetization phase carries a finite total angular momentum and is thus a chiral superfluid. Such an atomic chiral superfluid is reminiscent of the fermionic chiral superfluid in ^{3}He-A [37] or the chiral superconductor such as Sr_2RuO_4 [38], although in these fermionic systems the angular momenta are carried by the relative motion of Cooper pairs. Like these fermionic counterparts, the atomic chiral superfluid also gives rise to a nontrivial dichroic response [39,40]. To be specific, let us consider the responses of the system to two rotating potentials,

$$V_{\pm}(\boldsymbol{r}, t) = 2F(x\cos\omega t \pm y\sin\omega t), \tag{56}$$

where F is the force constant. Under such a perturbation, the excitation rate out of the ground state per unit area can be calculated by the Fermi's golden rule as [39,40]

$$W_{\pm}(\omega) = \frac{8\pi}{\hbar\mathcal{A}}\left(\frac{F}{\omega}\right)^2 \sum_n |\langle n|\hat{J}_{\pm}|0\rangle|^2 \delta(E_n - E_0 - \hbar\omega). \tag{57}$$

If the system is chiral, it naturally responds to the perturbations V_+ and V_- differently such that $W_+(\omega) \neq W_-(\omega)$. Defining the following integrated excitation rates:

$$W_{\pm,\mathrm{int}} \equiv \frac{\hbar}{4\pi F^2}\int_0^\infty d\omega W_{\pm}(\omega), \tag{58}$$

the difference of these two quantities in fact yields the real part of the dc Hall conductivity, namely [39,40],

$$\mathrm{Re}\,\sigma_H(0) = W_{+,\mathrm{int}} - W_{-,\mathrm{int}}. \tag{59}$$

Thus, this analysis shows that the system's chirality implies a finite dc Hall conductivity. To demonstrate this explicitly, we show in Fig. 12 the calculated $W_{\pm,\mathrm{int}}$ as a function of the SO-coupling strength, where we find $W_{+,\mathrm{int}} = W_{-,\mathrm{int}}$ for the in-plane magnetization phase while $W_{+,\mathrm{int}} > W_{-,\mathrm{int}}$ for the perpendicular magnetization phase.

B. Momentum-space perspective: Berry curvature

A complementary way of understanding the dc AHE in the atomic chiral superfluid is to make use of the relation between the dc Hall conductivity and the Berry curvature of the Bloch bands. In ferromagnetic materials where the anomalous Hall effect was originally discovered, the SO coupling gives rise to electronic bands with finite Berry curvatures, which can play the role of a magnetic field in deflecting the electrons moving under an electric field. The dc Hall conductivity is given by the summation of Berry curvatures of the occupied Bloch states. From this perspective, even a thermal gas of bosons in topologically nontrivial bands may exhibit the AHE [29,41,42].

Take the noninteracting bands in our SOC system as an example and suppose that fermions instead of bosons occupy these bands. The zero-temperature dc Hall conductivity would then be given by

$$\mathrm{Re}\,\sigma_H(0) = \frac{1}{\hbar\mathcal{A}}\sum_{n\boldsymbol{k}} \Omega_n(\boldsymbol{k}), \tag{60}$$

where the summation of $n, \boldsymbol{k}$ is restricted to the occupied Bloch states. Here, $\Omega_n(\boldsymbol{k})$ is the Berry curvature of the nth band,

$$\Omega_n(\boldsymbol{k}) = i(\langle\partial_{k_x}\mathfrak{u}_{n\boldsymbol{k}}|\partial_{k_y}\mathfrak{u}_{n\boldsymbol{k}}\rangle - \langle\partial_{k_y}\mathfrak{u}_{n\boldsymbol{k}}|\partial_{k_x}\mathfrak{u}_{n\boldsymbol{k}}\rangle), \tag{61}$$

where $\mathfrak{u}_{n\boldsymbol{k}}(\boldsymbol{r}) \equiv e^{-i\boldsymbol{k}\cdot\boldsymbol{r}}\boldsymbol{\phi}_{n\boldsymbol{k}}(\boldsymbol{r})$ and $\langle\partial_{k_x}\mathfrak{u}_{n\boldsymbol{k}}|\partial_{k_y}\mathfrak{u}_{n\boldsymbol{k}}\rangle$ is a shorthand notation for the inner product of the spinor wave functions, $\sum_\sigma \int d\boldsymbol{r}\partial_{k_x}\mathfrak{u}_{n\boldsymbol{k}\sigma}(\boldsymbol{r})\partial_{k_y}\mathfrak{u}_{n\boldsymbol{k}\sigma}(\boldsymbol{r})$. Now, because of the double

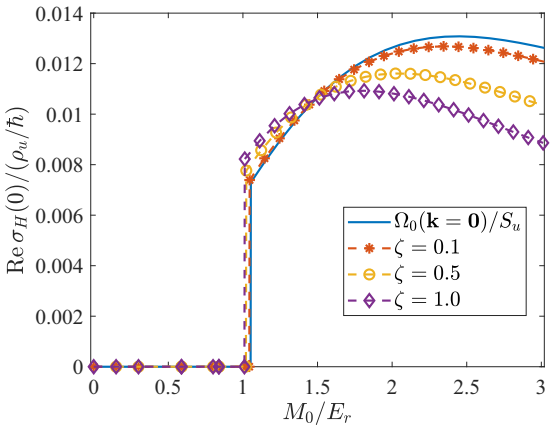

FIG. 13. The dc Hall conductivity as a function of M_0 for various values of interaction strengths. Here, $(\rho g_{\uparrow\uparrow}, \rho g_{\uparrow\downarrow}) = \zeta(0.35E_r, 0.3E_r)$. The solid line represents the right-hand side of Eq. (64).

degeneracy of the bands, the Berry curvature $\Omega_n(\boldsymbol{k})$ is actually ambiguous without specifying the Bloch wave function $\boldsymbol{\phi}_{n\boldsymbol{k}}(\boldsymbol{r})$. For spin-polarized states $\boldsymbol{\phi}^{\pm}_{m\boldsymbol{k}}$ introduced in Sec. III, the Berry curvatures are generally finite. Let us consider the bottom two bands as an example. If we take $\boldsymbol{\phi}_{0,\boldsymbol{k}} = \boldsymbol{\phi}^{+}_{0,\boldsymbol{k}}$ and $\boldsymbol{\phi}_{1,\boldsymbol{k}} = \boldsymbol{\phi}^{-}_{0,\boldsymbol{k}}$, we find

$$\Omega_0(\boldsymbol{k}) = -\Omega_1(\boldsymbol{k}) \neq 0. \tag{62}$$

On the other hand, for any state that is a superposition of $\boldsymbol{\phi}^{+}_{m,\boldsymbol{k}}$ and $\boldsymbol{\phi}^{-}_{m,\boldsymbol{k}}$ with equal weight, the Berry curvature is zero.

In our system, the origin of the dc Hall conductivity can also be discussed in this framework if we neglect the atomic interactions. The dc Hall conductivity in Eq. (29) can be written as

$$\begin{aligned}\mathrm{Re}\,\sigma_H(0) &= -\frac{1}{\mathcal{A}\hbar}\mathrm{Im}\sum_{n\neq 0}\frac{J_{x,0n}J_{y,n0} - J_{y,0n}J_{x,n0}}{(E_{n0}-E_{00})^2} \\ &= 2\frac{N}{\mathcal{A}\hbar}\sum_{n\neq 0}\frac{|\mathcal{J}_{+,n0}|^2 - |\mathcal{J}_{-,n0}|^2}{(\mathcal{E}_{n0}-\mathcal{E}_{00})^2},\end{aligned} \tag{63}$$

where the second line is obtained by the Bogoliubov theory. In the noninteracting limit, the above expression reduces to

$$\begin{aligned}\mathrm{Re}\,\sigma_H(0) &= -2\frac{N}{\mathcal{A}\hbar}\sum_{n\neq 0}\frac{\mathrm{Im}[\langle\boldsymbol{\phi}_{00}|p_x|\boldsymbol{\phi}_{n0}\rangle\langle\boldsymbol{\phi}_{n0}|p_y|\boldsymbol{\phi}_{00}\rangle]}{(\epsilon_{n0}-\epsilon_{00})^2} \\ &= \frac{\rho_u}{\hbar S_u}\Omega_0(\boldsymbol{k}=0),\end{aligned} \tag{64}$$

where S_u is the area of the Wigner-Seitz cell and ρ_u is the number of atoms per cell. This is exactly what we expect because all the atoms condensate at the same $\boldsymbol{\phi}_{00}$ state in the noninteracting limit. Since $\Omega_0(\boldsymbol{k}=0)$ is finite in the perpendicular magnetization phase and is zero in the in-plane magnetization phase, the difference in the dc Hall conductivities between these two phases can be immediately understood from the above equation. In Fig. 13, we have plotted $\mathrm{Re}\,\sigma_H(0)$ calculated for various values of $(\rho g_{\uparrow\uparrow}, \rho g_{\uparrow\downarrow}) = \zeta(0.35E_r, 0.3E_r)$, which clearly shows that the noninteracting result in Eq. (64) is recovered as $\zeta \to 0$.

Lastly, we comment on the difference between the AHE discussed in our bosonic system and that in fermionic systems such as the Haldane model. The first obvious difference is the quantum statistics. In our system of bosonic gas, all atoms occupy one particular state due to Bose condensation and so, as long as that state has nonzero Berry curvature, the system has a finite dc Hall conductivity. In contrast, the Haldane model consists of fermions and its dc Hall conductivity is given by the summation of Berry curvatures of the occupied states. In the case of a filled band, this summation corresponds to the Chern number of the band. Second, atomic interactions play a role in our system. As we have just seen from Fig. 13, the total dc Hall conductivity in our superfluid can be viewed as the contribution from the Berry curvature at the condensation state of the noninteracting band plus an interaction-induced correction. Such a correction does not exist in the AHE of the Haldane model as it consists of noninteracting fermions.

VI. EXPERIMENTAL PROPOSAL

Since the SOC condensate has already been realized in experiments, it is crucial to ask whether the predicted AHE can be detected with currently available experimental tools. In trapped atomic systems, it is difficult to directly measure the current response function and hence the Hall conductivity. In earlier discussions on the relation between chirality and the anomalous Hall effect, we have in fact shown earlier that the dichroism probe can be used to measure the dc Hall conductivity. In this section, we discuss an experimental method to probe the frequency dependence of the Hall conductivity and, in particular, to reveal the resonances exhibited in the Hall conductivity. The idea is to make use of a close relation between the current and the center-of-mass (COM) response functions, so that one can deduce the conductivity tensor from the responses of the COM to a time-periodic linear potential. This was first discussed in Ref. [27] and was later implemented experimentally to measure the longitudinal conductivity of a lattice Fermi gas [28].

To be more specific, let us consider the transverse response of the center-of-mass (COM) degree of freedom, $\hat{\boldsymbol{R}} = \frac{1}{N}\sum_\sigma \int \boldsymbol{r}\hat{\psi}^\dagger_\sigma(\boldsymbol{r})\hat{\psi}_\sigma(\boldsymbol{r})d\boldsymbol{r}$, to the following time-periodic linear potential:

$$V(\boldsymbol{r}, t) = -Fx\cos\omega t, \tag{65}$$

where F is the force constant. If the system has a finite Hall conductivity, such a force along the x direction will generate a response of the COM along the y direction. Within linear response theory, the COM response can be written as

$$\langle\hat{R}_y(t)\rangle = R_y(\omega)\cos[\omega t - \phi_y(\omega)], \tag{66}$$

where $R_y(\omega)$ is the amplitude and $\phi_y(\omega)$ is the phase lagging. It turns out that the finite-frequency Hall conductivity $\sigma_H(\omega)$ is related to the amplitude and phase of this response by [27]

$$\sigma_H(\omega) = \frac{N\omega}{i\mathcal{A}F}R_y(\omega)e^{i\phi_y(\omega)}. \tag{67}$$

Thus, by measuring the COM response along the y direction to the potential in Eq. (65), we can infer the ac Hall conductivity. Now, from Eq. (67) we may also calculate the expected

behavior of the COM response from knowledge of $\sigma_H(\omega)$. Inverting Eq. (67), we find

$$R_y(\omega) = \frac{\mathcal{A}F}{N\omega}|\sigma_H(\omega)|, \tag{68}$$

$$\phi_y(\omega) = \tan^{-1}\left[-\mathrm{Re}\,\sigma(\omega)/\mathrm{Im}\,\sigma(\omega)\right]. \tag{69}$$

In view of previous calculations of the Hall conductivity, we expect to find resonant behavior for the amplitude of the responses in both phases.

VII. CONCLUDING REMARKS

In this paper, we have calculated the finite-frequency Hall conductivity of a 2D SOC Bose gas at zero temperature in the absence of an artificial magnetic field, and we have demonstrated the existence of ground-state intrinsic anomalous Hall effects across the magnetic phase transition of the system. In the perpendicular magnetization phase, the SOC system realizes a chiral superfluid for which the ac Hall conductivity exhibits a behavior similar to that of a previously realized chiral superfluid in a boron nitride optical lattice. Namely, the real part of the ac Hall conductivity is reactive, while the imaginary part is absorptive. Importantly, we find a finite, albeit nonquantized, dc Hall conductivity in this phase. In contrast, it is exactly the opposite in the in-plane magnetization phase, where the ac Hall conductivity has an absorptive real part and a reactive imaginary part, and the dc Hall conductivity vanishes. In both phases, the ac Hall responses exhibit various resonances in frequency, which can be explained by the selection rules derived from the symmetry analysis. Furthermore, the contrast in the dc Hall conductivities of the two phases can be understood using the connection between the dc Hall conductivity and the chirality and the Berry curvature. Finally, we show that the AHEs discussed in this work can be readily probed experimentally by a measurement of COM responses of the condensate under a periodic driving. We expect that the amplitude of the COM motion will exhibit resonances at certain driving frequencies for the condensate in both magnetic phases. However, the difference in behavior of the frequency-dependent conductivity in the two phases will be reflected by the phase lagging of the COM motion since that latter is determined by the ratio of the real and the imaginary parts of the conductivity.

ACKNOWLEDGMENTS

This work is supported by National Key R&D Program of China (Grant No. 2022YFA1404103), NSFC (Grant No. 11974161), Shenzhen Science and Technology Program (Grant No. KQTD20200820113010023), and Key-Area Research and Development Program of Guangdong Province (Grant No. 2019B030330001).

[1] M. Z. Hasan and C. L. Kane, Colloquium: Topological insulators, Rev. Mod. Phys. **82**, 3045 (2010).
[2] X.-L. Qi and S.-C. Zhang, Topological insulators and superconductors, Rev. Mod. Phys. **83**, 1057 (2011).
[3] B. A. Bernevig and T. L. Hughes, *Topological Insulators and Topological Superconductors* (Princeton University Press, Princeton, NJ, 2013).
[4] D. J. Thouless, M. Kohmoto, M. P. Nightingale, and M. den Nijs, Quantized Hall Conductance in a Two-Dimensional Periodic Potential, Phys. Rev. Lett. **49**, 405 (1982).
[5] N. Nagaosa, J. Sinova, S. Onoda, A. H. MacDonald, and N. P. Ong, Anomalous Hall effect, Rev. Mod. Phys. **82**, 1539 (2010).
[6] D. Xiao, M.-C. Chang, and Q. Niu, Berry phase effects on electronic properties, Rev. Mod. Phys. **82**, 1959 (2010).
[7] N. R. Cooper, J. Dalibard, and I. B. Spielman, Topological bands for ultracold atoms, Rev. Mod. Phys. **91**, 015005 (2019).
[8] M. Aidelsburger, M. Atala, M. Lohse, J. T. Barreiro, B. Paredes, and I. Bloch, Realization of the Hofstadter Hamiltonian with Ultracold Atoms in Optical Lattices, Phys. Rev. Lett. **111**, 185301 (2013).
[9] H. Miyake, G. A. Siviloglou, C. J. Kennedy, W. C. Burton, and W. Ketterle, Realizing the Harper Hamiltonian with Laser-Assisted Tunneling in Optical Lattices, Phys. Rev. Lett. **111**, 185302 (2013).
[10] M. Atala, M. Aidelsburger, J. T. Barreiro, D. Abanin, T. Kitagawa, E. Demler, and I. Bloch, Direct measurement of the Zak phase in topological Bloch bands, Nat. Phys. **9**, 795 (2013).
[11] G. Jotzu, M. Messer, R. Desbuquois, M. Lebrat, T. Uehlinger, D. Greif, and T. Esslinger, Experimental realization of the topological Haldane model with ultracold fermions, Nature (London) **515**, 237 (2014).
[12] Z.-F. Xu, L. You, A. Hemmerich, and W. V. Liu, π-Flux Dirac Bosons and Topological Edge Excitations in a Bosonic Chiral p-Wave Superfluid, Phys. Rev. Lett. **117**, 085301 (2016).
[13] T. Kock, C. Hippler, A. Ewerbeck, and A. Hemmerich, Orbital optical lattices with bosons, J. Phys. B: At. Mol. Opt. Phys. **49**, 042001 (2016).
[14] X. Li and W. V. Liu, Physics of higher orbital bands in optical lattices: A review, Rep. Prog. Phys. **79**, 116401 (2016).
[15] M. Di Liberto, A. Hemmerich, and C. Morais Smith, Topological Varma Superfluid in Optical Lattices, Phys. Rev. Lett. **117**, 163001 (2016).
[16] T. Müller, S. Fölling, A. Widera, and I. Bloch, State Preparation and Dynamics of Ultracold Atoms in Higher Lattice Orbitals, Phys. Rev. Lett. **99**, 200405 (2007).
[17] G. Wirth, M. Ölschläger, and A. Hemmerich, Evidence for orbital superfluidity in the p-band of a bipartite optical square lattice, Nat. Phys. **7**, 147 (2011).
[18] P. Soltan-Panahi, D.-S. Lühmann, J. Struck, P. Windpassinger, and K. Sengstock, Quantum phase transition to unconventional multi-orbital superfluidity in optical lattices, Nat. Phys. **8**, 71 (2012).
[19] M. Ölschläger, T. Kock, G. Wirth, A. Ewerbeck, C. M. Smith, and A. Hemmerich, Interaction-induced chiral $p_x \pm ip_y$ superfluid order of bosons in an optical lattice, New J. Phys. **15**, 083041 (2013).
[20] T. Kock, M. Ölschläger, A. Ewerbeck, W.-M. Huang, L. Mathey, and A. Hemmerich, Observing Chiral Superfluid

Order by Matter-Wave Interference, Phys. Rev. Lett. **114**, 115301 (2015).

[21] M. Weinberg, C. Staarmann, C. Ölschläger, J. Simonet, and K. Sengstock, Breaking inversion symmetry in a state-dependent honeycomb lattice: Artificial graphene with tunable band gap, 2D Mater. **3**, 024005 (2016).

[22] W. Sun, B.-Z. Wang, X.-T. Xu, C.-R. Yi, L. Zhang, Z. Wu, Y. Deng, X.-J. Liu, S. Chen, and J.-W. Pan, Highly Controllable and Robust 2D Spin-Orbit Coupling for Quantum Gases, Phys. Rev. Lett. **121**, 150401 (2018).

[23] M. Hachmann, Y. Kiefer, J. Riebesehl, R. Eichberger, and A. Hemmerich, Quantum Degenerate Fermi Gas in an Orbital Optical Lattice, Phys. Rev. Lett. **127**, 033201 (2021).

[24] J. Vargas, M. Nuske, R. Eichberger, C. Hippler, L. Mathey, and A. Hemmerich, Orbital Many-Body Dynamics of Bosons in the Second Bloch Band of an Optical Lattice, Phys. Rev. Lett. **126**, 200402 (2021).

[25] X.-Q. Wang, G.-Q. Luo, J.-Y. Liu, W. V. Liu, A. Hemmerich, and Z.-F. Xu, Evidence for an atomic chiral superfluid with topological excitations, Nature (London) **596**, 227 (2021).

[26] C.-C. Chien, S. Peotta, and M. Di Ventra, Quantum transport in ultracold atoms, Nat. Phys. **11**, 998 (2015).

[27] Z. Wu, E. Taylor, and E. Zaremba, Probing the optical conductivity of trapped charge-neutral quantum gases, Europhys. Lett. **110**, 26002 (2015).

[28] R. Anderson, F. Wang, P. Xu, V. Venu, S. Trotzky, F. Chevy, and J. H. Thywissen, Conductivity Spectrum of Ultracold Atoms in an Optical Lattice, Phys. Rev. Lett. **122**, 153602 (2019).

[29] E. van der Bijl and R. A. Duine, Anomalous Hall Conductivity from the Dipole Mode of Spin-Orbit-Coupled Cold-Atom Systems, Phys. Rev. Lett. **107**, 195302 (2011).

[30] G.-H. Huang, Z.-F. Xu, and Z. Wu, Intrinsic Anomalous Hall Effect in a Bosonic Chiral Superfluid, Phys. Rev. Lett. **129**, 185301 (2022).

[31] G.-H. Huang, G.-Q. Luo, Z. Wu, and Z.-F. Xu, Interaction-induced topological Bogoliubov excitations in a spin-orbit-coupled Bose-Einstein condensate, Phys. Rev. A **103**, 043328 (2021).

[32] J.-S. Pan, W. Zhang, W. Yi, and G.-C. Guo, Bose-Einstein condensate in an optical lattice with Raman-assisted two-dimensional spin-orbit coupling, Phys. Rev. A **94**, 043619 (2016).

[33] J. F. Cornwell, *Group Theory in Physics* (Academic Press, San Diego, CA, 1984), Vol. 1.

[34] M. S. Dresselhaus, G. Dresselhaus, and A. Jorio, *Group Theory: Application to the Physics of Condensed Matter* (Springer Science & Business Media, New York, 2007).

[35] H. Zhai, Degenerate quantum gases with spin-orbit coupling: A review, Rep. Prog. Phys. **78**, 026001 (2015).

[36] This phase transition can be viewed as a stripe-to-plane-wave phase transition with respect to the transformed Hamiltonian $\hat{H}' = U\hat{H}U^{-1}$.

[37] H. Ikegami, Y. Tsutsumi, and K. Kono, Chiral symmetry breaking in superfluid ^{3}He -A, Science **341**, 59 (2013).

[38] C. Kallin and J. Berlinsky, Chiral superconductors, Rep. Prog. Phys. **79**, 054502 (2016).

[39] D. T. Tran, A. Dauphin, A. G. Grushin, P. Zoller, and N. Goldman, Probing topology by "heating": Quantized circular dichroism in ultracold atoms, Sci. Adv. **3**, e1701207 (2017).

[40] J. M. Midtgaard, Z. Wu, N. Goldman, and G. M. Bruun, Detecting chiral pairing and topological superfluidity using circular dichroism, Phys. Rev. Res. **2**, 033385 (2020).

[41] A. M. Dudarev, R. B. Diener, I. Carusotto, and Q. Niu, Spin-Orbit Coupling and Berry Phase with Ultracold Atoms in 2D Optical Lattices, Phys. Rev. Lett. **92**, 153005 (2004).

[42] Y. Li, P. Sengupta, G. G. Batrouni, C. Miniatura, and B. Grémaud, Berry curvature of interacting bosons in a honeycomb lattice, Phys. Rev. A **92**, 043605 (2015).